OPTICS

Combinatorial optimization with Kerr solitons

Yan Jin[1,2]*, Nitesh Chauhan[1,2]†, Jizhao Zang[1,2], Brian Edwards[3], Pratik Chaudhari[3], Firooz Aflatouni[3], Scott B. Papp[1,2]*

The challenge of scaling digital computing motivates innovation, especially through the evolution of physical systems that mimic neural networks and combinatorial optimization problems. Light is a hyperefficient information carrier, and if efficient interactions with it could be uncovered, then direct information processing would become far more feasible. We harness an ensemble of hundreds of Kerr microresonator solitons and implement an analog feedback network to create an Ising machine with fully programmable all-to-all interactions. By increasing the feedback for self, on-diagonal interactions, each soliton exhibits a universal spin-like bifurcation, and using this palette of interactions, we solve the canonical Boolean satisfiability problem (SAT). The combination of uniform soliton interactions and the compatibility of our Ising machine with high-speed data interconnects enables rapid and precise solutions of complex SAT problems. The well-established theoretical properties of Kerr solitons bound the trade-off of optical power and time use by the machine at ~0.15 milliwatts per soliton and 1 microsecond for a single feedback step. We performed >10,000 trials on more than 100 randomly generated SAT instances to evaluate the Ising machine, demonstrating the potential to exceed the performance of benchmark digital SAT solvers. Our work highlights the convergence of optical nonlinearity, ultralow loss photonics, and optoelectronic circuits for computation-acceleration tasks.

INTRODUCTION

The end of rapid scaling in digital-computer technology and the rise of machine optimization and artificial intelligence have opened interest in controllable and scalable physical systems to solve combinatorial optimization problems, which are widely used in schedule optimization, finance, chemical discovery, and deep neural network architectures (*1*–*7*). In particular, physical approaches leverage quantum-inspired behaviors such as discrete spin interactions, featuring sharp state transitions and the potential for scalable spin networks with low operation power.

Boolean satisfiability (SAT) is the canonical NP-complete (nondeterministic polynomial-time complete) example, meaning that every problem in NP can be efficiently reduced to SAT, and thus, SAT serves as a central benchmark. Therefore, numerous non–von Neumann architectures have been explored to solve these problems by mapping them to an Ising model. An extraordinary range of physical systems can be arranged to create an Ising machine, notably parametric oscillators (*8*–*10*), spatial light modulators (*11*, *12*), photonic integrated circuits (*13*), opto-electronic networks (*14*–*16*), Kerr nonlinear optics (*17*), electronic circuits (*6*, *18*), nonlinear polarization oscillators (*19*), and complementary metal-oxide semiconductor (CMOS) circuits with static random-access memory (SRAM) (*20*).

Despite their connection with interacting quantum-spin systems, Ising machines are implemented with a range of architectures in which memory, connectivity, interaction speed, and scalability are key. A notional digital/analog electronic circuit can implement an Ising machine in which pristine spin states are stored in a digital SRAM array. Connectivity is realized through multiplexing of analog current signals derived from the SRAM. Nonlinearity is introduced via comparators that project the analog interaction sum back into discrete digital spin states, closing the feedback loop. However, the power consumption of digital-to-analog and analog-to-digital converters, the latency in SRAM access, and the signal propagation delay in comparators impose fundamental limits on update throughput and ultimately constrain the overall spin capacity and performance of these hybrid systems. These ubiquitous CMOS constraints motivate the exploration of alternative physical substrates such as photonics that promise lower energy per operation and far greater parallelism.

Kerr-microresonator solitons are discrete and localized electromagnetic excitations of an intraresonator field, exhibiting dissipation, gain, and the balance of nonlinearity and phase matching (*21*–*23*). These solitons exhibit modelocking, and they form an outcoupled, ultrafast optical pulse train from the resonator that we associate with an optical frequency comb. Hence, we refer to this system as a soliton microcomb, and it exhibits extraordinary optical and microwave coherence with fractional optical frequency accuracy and precision reaching 10^{-20} (*24*), which supports applications ranging from optical frequency metrology (*24*) to optical data interconnects to universal electronic synthesis (*25*). From the earliest experiments with Kerr solitons, their discreteness was recognized, and ensembles of solitons feature a high degree of indistinguishability and long-range interactions (*26*). Moreover, soliton microcombs can be implemented with increasingly advanced photonic integration technologies (*27*) and foundry manufacturing (*28*).

Here, we introduce a Kerr-soliton Ising machine and use it to solve combinatorial optimization problems. We implement the Ising machine with a large ensemble of Kerr solitons in a resonator, and we map fully programmable all-to-all interactions among the ensemble with an opto-electronic feedback network. The emergent collective state of the discrete solitons represents the spins of the Ising model, and we program the hybrid opto-electronic feedback network to directly couple SAT instances, multiplexing the solitons in time and among one electrical path for each optimization problem mapped to the Ising model. The soliton spin bifurcation arises directly from Kerr nonlinearity because there are only two, distinct,

[1]Time and Frequency Division, National Institute of Standards and Technology, Boulder, CO USA. [2]Department of Physics, University of Colorado, Boulder, CO, USA. [3]Department of Electrical and Systems Engineering, University of Pennsylvania, Philadelphia, PA, USA.
*Corresponding author. Email: yan.jin@nist.gov (Y.J.); scott.papp@nist.gov (S.B.P.)
†Present address: Nokia of America Corporation, Sunnyvale, CA, USA.

quantum-based eigenstates of the resonator (*29*), the empty state and the soliton state. To evolve the Ising machine, we photodetect the soliton spin states and use stepped gradient descent to update the feedback circuit. Each step fundamentally requires 3.5 μs of time in accord with the soliton nonlinear dynamics. Moreover, each soliton only consumes around 2.3 mW of pump power in the present apparatus. Hence, we can solve complex, arbitrary SAT problems more rapidly and with two orders of magnitude less optical energy than benchmark digital computer algorithms. Furthermore, the Kerr soliton Ising machine shows low latency, rapid execution, energy efficiency, and good stability and scalability.

RESULTS

The concept of our Kerr soliton Ising machine is shown in Fig. 1A, including a high finesse Kerr resonator (circle) to generate solitons and a low finesse feedback network (oval) to mediate all-to-all soliton interactions. Kerr solitons propagate endlessly in a resonator without temporal spreading, and each spatial coordinate of the resonator can support at most one soliton. Moreover, as we increase the pump power, there is a sharp transition from the empty state to the soliton. Each of the solitons (blue) is excited by the corresponding pump pulses (orange) coupled from an external path. We model the behavior of solitons with the Lugiato-Lefever equation (LLE) (*30*), including use of the Kerr soliton Ising machine to solve 3-SAT problems (see Materials and Methods). The intracavity field $a(\theta_i)$ for each of the N solitons is controlled by a repeating sequence of incoming pump pulses $f(\theta_i)$, where θ_i ranges from $2\pi i/N$ to $2\pi(i+1)/N$. The LLE solutions indicate that the two states of the solitons, i.e., either excited or empty, are two nonlinear eigenstates, and the blue traces on top of a circular ring in Fig. 1A show the multisoliton ensemble in a resonator mapped into mathematical spins in the Ising model. The Hamiltonian or Ising energy is

$$H = \boldsymbol{\sigma}^{\mathrm{T}} \cdot \mathbf{J} \cdot \boldsymbol{\sigma} + \mathbf{h} \cdot \boldsymbol{\sigma} = \sum_{i,j} J_{ij}\sigma_i\sigma_j + \sum_i h_i\sigma_i \tag{1}$$

where $\boldsymbol{\sigma}$ is the Ising spin array with $\sigma_i \in \{-1, 1\}$ being the ith spin, $\mathbf{J}$ is the interaction matrix with J_{ij} being its element, and $\mathbf{h}$ is the external force array with h_i the elements. Inside the resonator, the spin is up ($\sigma_i = 1$, marked with red arrows) if the soliton is excited and if the peak of its power within $[2\pi i/N, 2\pi(i+1)/N]$ reaches a given value $|a_0|^2$, and down ($\sigma_i = -1$, marked with blue arrows) otherwise.

While the solitons provide a highly robust physical platform to mimic spin behavior, the operational key to information processing in the Ising machine is the external feedback network. Outcoupled solitons are multiplexed and modulated with a time-domain signal through a feedback circuit (ξ in Fig. 1A) to program $\mathbf{J}$. The feedback circuit acts through the intensity of the pump pulses, and we present its architecture in more detail in Fig. 1B, with the feedback circuit and the pump laser shown in green and orange boxes, respectively. In the feedback circuit, we realize hybrid multiplexing of solitons through propagation in N paths and by application of time dependent attenuation of the paths. Operationally, we photodetect the soliton intensity $|a(\theta_i)|^2$ from the drop port of the resonator, apply a preset bias $|a_0|^2$ to bifurcate two soliton spin levels $\sigma'_i \propto |a_i|^2 - |a_0|^2$, where $|a_i|^2$ is the peak of $|a(\theta_i)|^2$ (see Materials and Methods). While mathematical spins σ_i are discrete, σ'_i are continuous and range approximately from −1 to 1. We decide the value of σ_i by the sign of σ'_i. To drive the Ising machine system toward its minimum energy, we perform a gradient-descent update on each spin. The feedback term has the form of $\xi_i = \eta\left(-2\sum_j J_{ij}\sigma'_j - h_i\right)$ from Eq. 1,

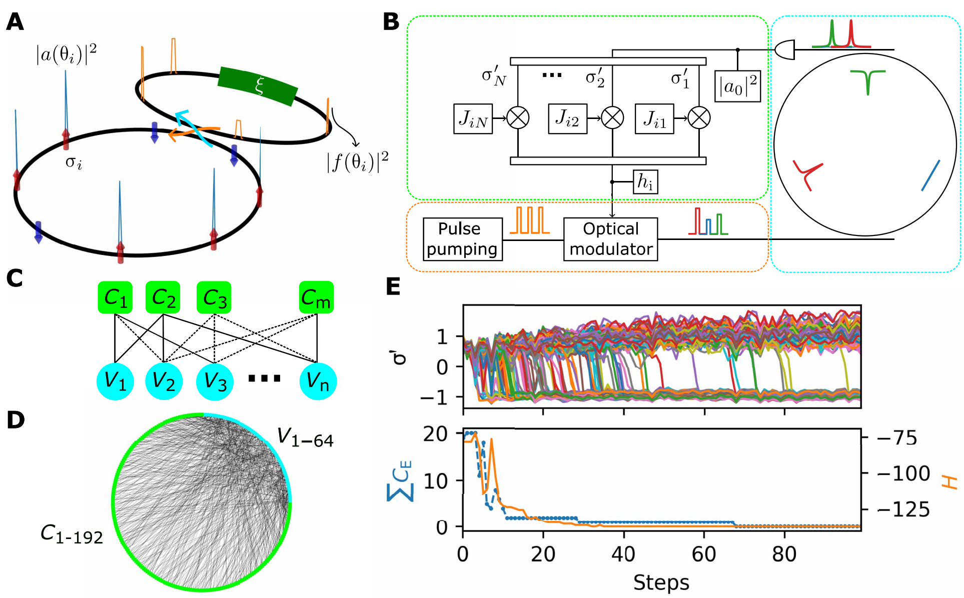

Fig. 1. Kerr soliton Ising machine. (**A**) Resonator with soliton spins (circle) and the feedback network with the pump and the feedback circuit (oval). Pump pulses (orange) and solitons (blue) are described by $|f(\theta_i)|^2$ and $|a(\theta_i)|^2$ in the spatial domain, respectively, and ξ refers to the feedback circuit. (**B**) Schematic of the Ising machine, including the feedback circuit (green box), the soliton resonator and photodetection (blue box), and the pump (red box). (**C**) Structure of a 3-SAT problem, where V_i ($i \in \{1, 2, \ldots n\}$) and C_i ($i \in \{1, 2, \ldots m\}$) are variables and clauses, respectively. The solid lines connect variables, and dashed lines connect the negation of variables. (**D**) 3-SAT problem with 64 variables and 192 clauses. (**E**) Evolution of the Ising machine versus gradient-descent step for the 3-SAT problem in (D). In the top panel, the soliton spins bifurcate to two states. In the bottom panel, the number of unsatisfied clauses $\sum C_E$ and the Hamiltonian H evolve to the global minimum.

where η denotes an overall attenuation factor. The Ising machine approaches steady state due to nonlinear soliton evolution and this per soliton feedback. Because ξ_i directly changes the corresponding pump field $f(\theta)$, we add the external force h_i without relation to the spins σ_i'. Thus, the number of required solitons is the number of spins in the Ising model, whereas in other Ising machines such as the coherent Ising machine, addtional spin sources or computational costs are required to apply h_i (*3*, *31*) (see the "Driving force of the Kerr soliton Ising machine" section in Materials and Methods for detailed explanation).

To form ξ_i for the soliton spin at site i, we multiply each of σ_i' with the fixed interaction term $2J_{ij}$ in each path, combine them, and bias the combined signal with h_i. This represents one $\mathcal{O}(N^2)$ matrix-vector multiplication. We generate an electronic waveform with ξ_i and apply it to the optical modulator in the same order as the soliton sequence in the time domain. With time and path multiplexing, the feedback network realizes all-to-all interactions and individually addresses the solitons at each site. The size of the feedback network scales linearly with the number of soliton spins N, indicating that our system can scale up to address even larger optimization problems.

We coordinate operation of the solitons and the feedback network with the pump laser and the photodetector (see the blue box in Fig. 1B). We generate temporally broad pump pulses (orange) and then adjust the intensity of each pulse to be $|f(\theta_i)|^2 = |f_0(\theta_i)|^2(1+\xi_i)$ with the optical modulator, where $f_0(\theta_i)$ is chosen such that $|a_i|^2 \simeq |a_0|^2$ (see Materials and Methods). All the pump pulses couple to the Kerr resonator, and we characterize $|f(\theta_i)|^2$ in terms of the threshold power to generate a soliton. The solitons in the Kerr resonator evolve at the timescale of the photon lifetime, which is 0.3 μs, and the soliton ensemble is efficiently outcoupled from the resonator for photodetection. The closed-loop feedback computes the effective field acting on each spin, derived from the gradient of the programmed Ising Hamiltonian, and applies pump modulations that bias the soliton toward the lower-energy state. Thus, the stable points of the hybrid system correspond to local minima of H, as confirmed by the monotonic decrease of the measured Ising energy during evolution (see Materials and Methods).

We benchmark the performance of the Kerr-soliton Ising machine by solving arbitrary, randomly generated SAT problems. Boolean satisfiability is a decision problem about whether a Boolean formula can be satisfied by assigning truth values to its variables. A problem (Fig. 1C) consists of n variables V_i ($V_i \in \{\text{True}, \text{False}\}$) and m clauses C_i ($C_i \in \{\text{True}, \text{False}\}$), which are the logical operator OR of the variables or their negation. Specifically, we solve 3-SAT problems in which each clause contains three variables or their negation. Figure 1C presents an example 3-SAT problem with the variable nodes along a blue circle and the clause nodes in a green square. We use the solid line when a variable is in a clause and the dashed line when the negation of a variable is in a clause. For example, the clause node C_1 is connected to V_1 and V_3 with solid lines, and to V_2 with dashed lines, thus can be written as $C_1 = (V_1 \vee \neg V_2 \vee V_3)$, where $\neg V_2$ is the negation of V_2. If V_1 and V_3 are false and V_2 is true, and then clause C_1 is unsatisfied. We define the number of unsatisfied clauses as $\sum C_E$. To solve the 3-SAT problem with the Ising machine, we first translate it into a quadratic unconstrained binary optimization (QUBO) problem (*32*) and then convert it to an Ising model with an efficient algorithm on a digital computer. A 3-SAT problem with n variables and m clauses can be transformed into an Ising problem with $N = m + n$ spins, and finding the ground state of the Ising problem is equivalent to finding the solution to the 3-SAT problem, i.e., a set of V_i such that the Boolean formula $C_1 \wedge C_2 \wedge \ldots C_m$ is satisfied and $\sum C_E = 0$.

Figure 1D demonstrates the use of the Kerr soliton Ising machine to solve a 3-SAT problem that contains $n = 64$ variables and $m = 192$ clauses. We translate this problem to an Ising model with $N = 256$ spins and encode the interaction matrix $\mathbf{J}$ and external field $\mathbf{h}$ to the feedback circuit. The computation begins with a setting $\eta = 0$ and injection of a train of pump pulses with uniform intensity. We photodetect the soliton spins σ_i' to obtain the feedback term ξ_i and modulate the peak power of pump pulses with ξ_i, which completes the first step of gradient descent. Then, we gradually increase η until the Ising machine runs a certain number of steps N_s to reach the final state. The choice of N_s is crucial because sufficient steps are needed to reach a stable minimum of the Ising energy. For this problem, we take $N_s = 100$ steps to drive the Ising machine to the final state.

Figure 1E presents the evolution of the spin values σ', the corresponding Ising energy H, and the number of unsatisfied clauses $\sum C_E$ with each step. As we increase η from 0, the soliton spins are strongly projected to two, distinct stable states—either excited or empty—and H and $\sum C_E$ converge to a minimum. As $\sum C_E$ reaches zero, all the clauses are satisfied for a complete solution of the 3-SAT problem. The noise of the solitons is not large enough to flip the solitons spins σ_i', but since ξ_i has the combination of N σ_i', the noise is strong enough to randomly flip σ_i' that are close to 0, which leads the system to choose different trajectories as we restart. Thus, although we have spins all up for the initial states, the results are still probabilistic. Gradient descent applied to the Ising model is inherently probabilistic, as the nonconvex energy landscape of the Ising interaction leads to local minima and no guarantee of convergence to the global minimum. Therefore, we perform repeated trials of the machine, testing each trial for $\sum C_E = 0$. The soliton amplitude bifurcation that enables our Ising machine arises from feedback-induced bistability of the soliton field due to Kerr nonlinearity, providing a physical representation for discrete spin states. The machine works for a wide range of η, as sharp soliton state transitions (Fig. 1E) occur with the increase of η from zero. This result aligns with the prediction from the LLE (see Materials and Methods) (*30*).

To investigate the soliton spin bifurcation, we program an on-diagonal self-interaction Hamiltonian ($J_{ij} = J_{ii}\delta_{i,j}$) with off-diagonal terms zero, as shown schematically in Fig. 2A. We set η as a nonzero constant and vary the diagonal terms J_{ii} from −1 to 1, which effectively creates a train of pump pulses with increasing intensity. To explore the response under different conditions, we select $N = 64$, 128, and 256 soliton states in a round trip, as shown in Fig. 2B, and for each N, we vary η to prepare three different self-interacting Hamiltonians to generate the feedback ξ_i within three different ranges: $\xi_i \in [-1, 1]$, $\xi_i \in [-0.8, 0.8]$ and $\xi_i \in [-0.7, 0.7]$. These ranges correspond to the green, red, and blue datasets in Fig. 2B. For each experimental setting of ξ_i, we measure σ' (dots) and fit the data with the sigmoidal function (dashed line). We adjust $|a_0|^2$ to ensure that the soliton state reaches the threshold when the feedback $\xi = 0$ (gray dashed line) and assign spin-up ($\sigma_i = 1$) in the red arrow region or spin-down ($\sigma_i = -1$) in the blue arrow region based on the sign of σ_i'. Before we run the Kerr soliton Ising machine, we calibrate the $|f_0(\theta)|^2$ and $|a_0|^2$ with the sigmoid fitting presented in Fig. 2. We note that J_{ii} is a preset constant as we run the Ising machine, and we vary J_{ii} here merely for characterizing the system. The soliton states σ' present a slightly stronger bifurcation with larger ξ, which likely results from saturation of the photodetector and erbium-doped fiber amplifier

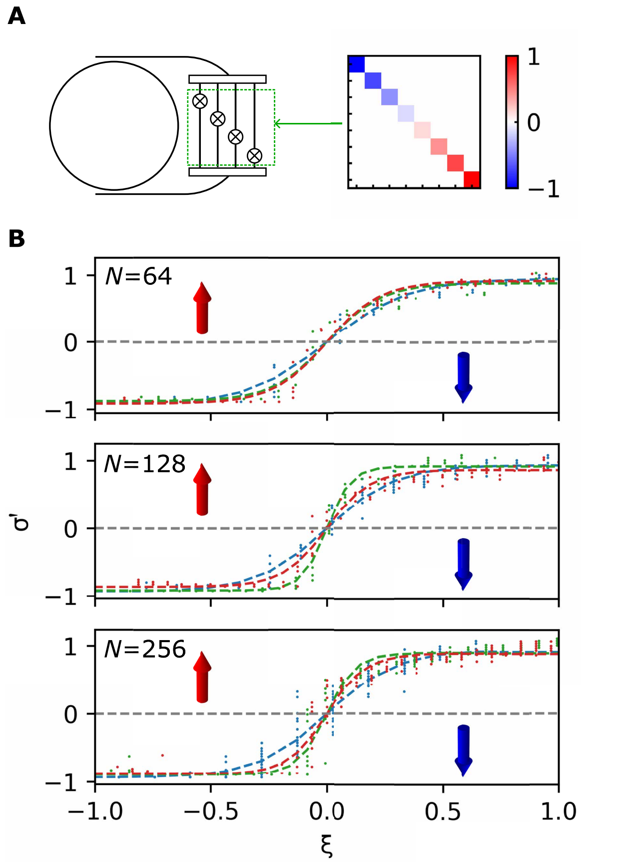

Fig. 2. Universal spin bifurcation in Kerr solitons. (**A**) Feedback with self interaction. The diagonal **J** matrix is sent to the feedback circuit of the Ising machine system to realize the self interaction. (**B**) Nonlinearity with $N = 64$, 128, and 256 soliton states in one round trip. For each N, we set different feedback ranges $\xi \in [-1, 1]$ (green), $[-0.8, 0.8]$ (red), and $[-0.7, 0.7]$ (blue). The dots are measured data points, and the dashed lines are the fitting.

(EDFA). In our experiments, the observed bifurcation predominantly originates from the Kerr nonlinearity of the soliton field. The universal bifurcation behavior of the solitons across a wide range of pump powers and experimental conditions ensures robust spin-state discrimination, serving as a key enabler for efficient and scalable SAT problem solving in the Kerr-soliton Ising machine. Because of the noise in the system, the soliton spin states tend to be more unstable at the threshold $\xi_i \simeq 0$. We discuss the role of the noise in the Supplementary Materials.

We present the experimental setup of the soliton Ising machine in Fig. 3A. The pump laser, feedback circuit, and the Kerr resonator are highlighted in orange, green, and blue, respectively. For the pump, a 1556-nm laser is the source for Pound-Drever-Hall (PDH) locking and pulse-pump generation using an electro-optic frequency comb driven at 7.4 GHz by a phase modulator (PM) and an intensity modulator (IM1) (*24*, *33*).

We use a separate intensity modulator (IM2) to close the feedback circuit from the PD to the pump-pulse intensity. Operationally, in the feedback circuit we photodetect the soliton intensities, digitize $|a_i|^2 - |a_0|^2$, and use a computer to generate an electrical waveform with a 20-GHz bandwidth that applies ξ_i (see Materials and Methods). The pump pulses are amplified by an EDFA and injected into the fiber resonator. We use a circulator to measure the reflected power for PDH locking. We generate solitons in a 25-m single-mode fiber (SMF) resonator with a round trip of $T_r = 138$ ns. The resonator incorporates two SMF couplers: one with coupling ratio of 90:10 for injecting the pump pulses into the resonator and one with 99:1 ratio for extracting the soliton spins and monitoring the PDH locking state. We pump the resonator with a train of pulses with linearly increasing intensity as in Fig. 2 to record the site of each soliton state and calibrate $|a_0|^2$ with $\sigma' \simeq 0$, when $\xi = 0$. During each gradient-descent step of a machine run, we calculate the feedback $\xi_i = \eta\left(-2\sum_j J_{ij}\sigma'_j - h_i\right) \propto -\mathrm{d}H/\mathrm{d}\sigma'_i$ and update $f(\theta_i)$, which precisely mimics the behavior of a path-multiplexed electronic circuit.

The scalability of the soliton spin number is an important advantage of our Ising machine because this enables the solution of larger optimization problems. Figure 3B demonstrates generation of a $N = 256$ soliton ensemble within one round trip of the resonator, leveraging 256 independently programmable pump pulses. The average power of the pulsed-pump laser naturally scales with N, which we characterize in Fig. 3C. We measure the minimum, threshold optical power required to create the soliton ensemble as we vary N, demonstrating 2.3 mW, which is comparable to the predicted threshold 0.9 mW (see Materials and Methods). In our experiments when solving 3-SAT problems, we set the EDFA power to twice the threshold.

The rapid evolution of Kerr solitons is a key feature of the Ising machine. We record the full dynamics of the solitons in the time domain with the oscilloscope when solving an Ising problem with $N = 256$ spins, as shown in Fig. 3D. We repeatedly send 80 round trips of pump waveforms $|f(\theta)|^2$ (orange) at each gradient descent step, where the pump pulses in the first 40 round trips are replicated to continuously excite the solitons at the corresponding sites, and the waveform in the last 40 round trips is null to maintain a buffer between the rapidly repeated runs of the machine (see Materials and Methods). We measure the soliton waveform $|a(\theta)|^2$ (blue) and align the start of the pump and soliton waveforms. In the beginning, the soliton intensity is low. The solitons gradually evolve to a steady state with continuous pulse pumping and fade away as we turn off the pump. We present two stages of solitons during a single step: two round trips of initial build-up in stage (i) and one round trip of the stable state in stage (ii). As the system evolves, the peak power of the solitons in each round trip gradually increases until they reach a constant value. It requires more time to accumulate the power in the fiber resonator and generate solitons for some pump pulses with lower power. Therefore, the stable state of stage (ii) contains more solitons despite the fact that the peak power in stage (i) is comparable to that in stage (ii). The operation time during which the solitons become stable depends fundamentally on the external coupling rate, which we can control by changing the couplers with different coupling ratios.

We explore the use of the Kerr soliton Ising machine to solve arbitrary, randomly generated 3-SAT problems, benchmarking the machine in terms of unit-normalized solution probability (P) and the time to solution (TTS) (see Fig. 4). Since 3-SAT is NP-complete, there do not exist polynomial-time deterministic solvers, and probabilistic approaches, e.g., our Ising machine and the widely used benchmark WalkSAT algorithm (*34*, *35*), require repeated trials to search the vast solution space. First, we characterize the dependence of P on N_r, which represents the amount of time per gradient-descent

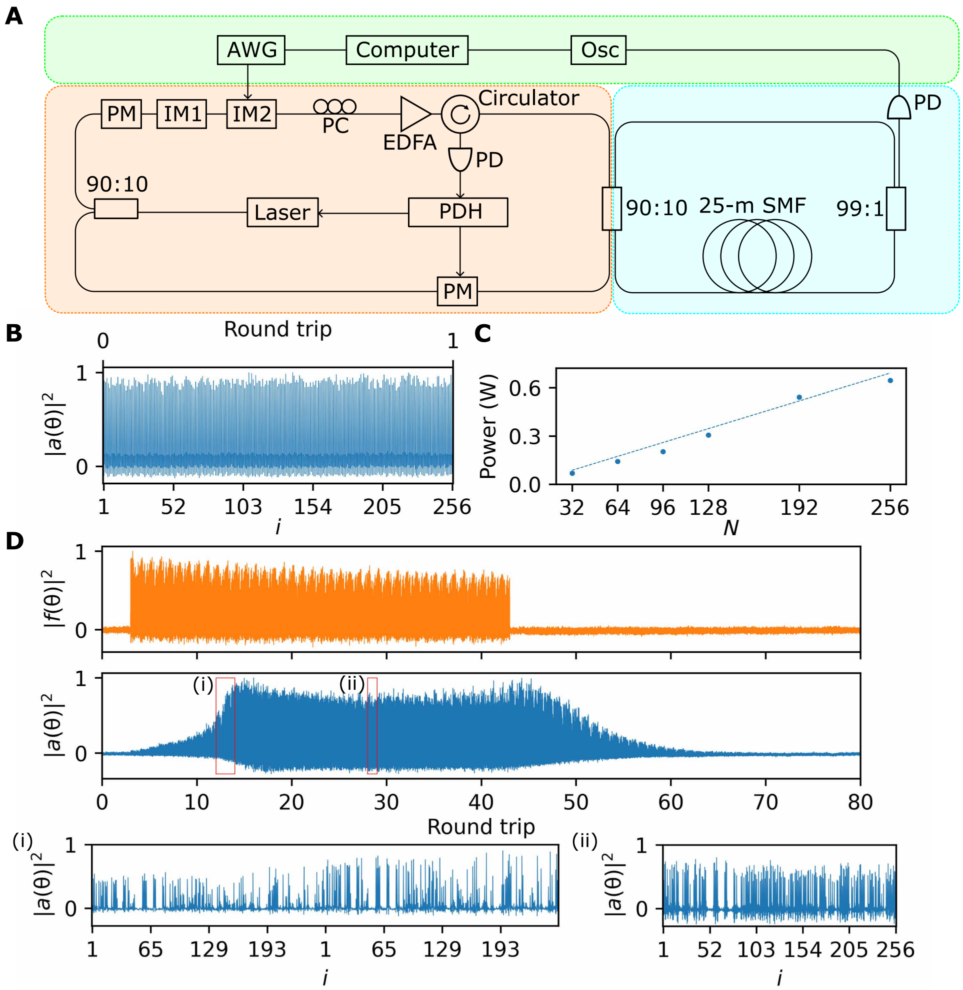

Fig. 3. Experimental setup and evolution of soliton ensembles. (**A**) Setup. PM, phase modulator; IM, intensity modulator; AWG, arbitrary waveform generator; Osc, oscilloscope; PD, photodetector; PDH, Pound-Drever-Hall locking; EDFA, Erbium-doped fiber amplifier; PC, polarization controller; SMF, single-mode fiber. (**B**) Intracavity field intensity $|a(\theta)|^2$ for $N = 256$ solitons in a round trip. (**C**) Minimal EDFA power required to generate solitons for different N. (**D**) Pump pulses (orange) and solitons (blue) in a step. The pump is on for 40 round trips and off for another 40 round trips. The corresponding solitons evolve to a stable state and fade after the pump is off. Stage (i) presents two round trips of solitons during initial build-up, and stage (ii) presents one round trip of solitons at the stable state.

step that the solitons are active in problem solution. For a 3-SAT problem with $n = 85$ and $m = 171$, we map it to the Ising Hamiltonian with $N = 256$ with the procedure in (32) by the use of a digital computer. Similar to the procedure of Fig. 3D for operation of the Ising machine, we define a repeated pump-pulse sequence of 80-T_r duration with 50% duty cycle that initiates solitons and evolves the system with the J_{ij} interaction. Repeated trials of the pulse sequence search for solutions randomized by fluctuations in the solitons. To characterize P, we vary the setting of N_r, which defines the evolution time of the soliton intensities $|a(\theta_i)|^2$ for each step of gradient descent. The solution probability saturates, and we fix $N_r = 25$ for all of the experiments reported in this paper. This corresponds to a time of $T_s = N_r T_r = 3.5\ \mu s$ for each step of gradient descent, which is the essential contribution to TTS, traceable to the LLE, and represents a fundamental trade-off in power consumption and TTS (see Materials and Methods).

Figure 4B explores the results of 100 full runs of the Ising machine, including time for T_s evolution and readout and N_s gradient-descent steps for a single, randomly generated 3-SAT problem instance with $n = 64$ variables and $m = 192$ clauses. We characterize the Ising energy H versus $\sum C_E$ and the histogram of $\sum C_E$ for the initial (red) and final (green) soliton spin configuration. For a 3-SAT problem, each clause has three variables or their negations, and thus, there is a probability of one-eighth to be false for a random trial solution. Because there are 192 clauses, the number of unsatisfied clauses in the random, initial soliton spins is ~24. After each complete run of the Ising machine, the final states mostly have less than six unsatisfied clauses with $P = 5\%$ of them satisfying all clauses, i.e., $\sum C_E = 0$. This demonstrates the effectiveness of the Ising machine to solve these complex, NP-complete 3-SAT problems. For random 3-SAT problems, P declines with the problem size (n) and the clause-to-variable ratio (m/n) (36, 37), which affects the time and energy consumed by the Ising machine to reach the solution.

To benchmark the efficiency of 3-SAT solutions with the Kerr soliton Ising machine, we characterize P, TTS, and the energy to solution (ETS), which are standard metrics convertible between a

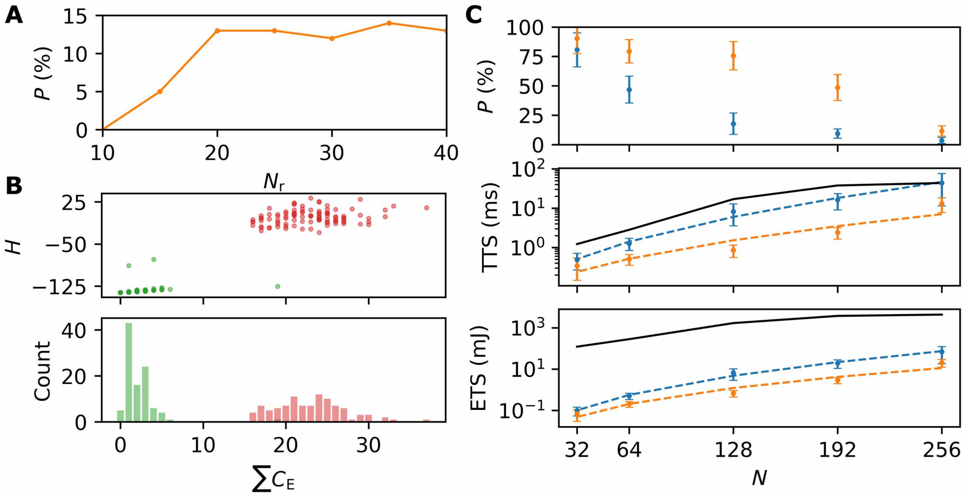

Fig. 4. Performance of Kerr soliton Ising machine. (**A**) Success probability P with different N_r. (**B**) Ising energy landscape and distribution of number of unsatisfied clauses $\sum C_E$. The red dots indicate the Ising energy H and number of unsatisfied clauses $\sum C_E$ in the initial state, and the red bars indicate the initial conditions. The green dots and bars are for final states. (**C**) Success probability (P), TTS, and ETS for different numbers of spins N and for different problem difficulty (orange for $m/n = 2$ and blue for $m/n = 3$). The dashed lines are the fitting, and the error bars denoting one SD of the data are calculated from results of five different problems for each N. The black curves are results using the WalkSAT algorithm.

wide range of 3-SAT solvers. We define TTS as the time to reach $\sum C_E = 0$ with 99% probability

$$\mathrm{TTS} = T_s N_s \frac{\log(1-0.99)}{\log(1-P)} \tag{2}$$

This measure of TTS considers the evolution time of solitons, hence the on time of the solitons, and excludes the calculation time of the feedback and the time to update the feedback. A machine copackaged with an integrated opto-electronic controller would be limited to this TTS. The other metric is ETS, which is defined as the energy consumed during the TTS. For a probabilistic 3-SAT solver, these metrics depend on problem size, hence the requirement for N, and problem complexity. In Fig. 4C, we show P, TTS, and ETS as a function of $N = 32$, 64, 128, 192, and 256 and $m/n = 2$ (orange) and 3 (blue), respectively. For each N and m/n, we generate five, random 3-SAT problems and run the problems 100 times using the number of gradient-descent steps specified in Materials and Methods. The success probability (Fig. 4C) varies slightly, as indicated by the intervals on the data markers, for different 3-SAT instances, and it depends substantially on both N and m/n. For $m/n = 3$ (blue dots), P decreases exponentially, while for $m/n = 2$ (orange dots), P decreases slowly for $N \leq 128$ because these problems are relatively simple to solve and decays more rapidly for $N > 128$. A lower success probability P implies longer time and higher energy consumption to reach the solution. The middle and bottom panels of Fig. 4C present the corresponding TTS and ETS, respectively. TTS and ETS increase with m/n and N. We fit the data points to $e^{\sqrt{N}}$ (see the dashed lines in Fig. 4C). Given the number of instances and the scatter of the data, these fits should be interpreted as suggestive of the overall scaling behavior of the Kerr soliton Ising machine using a representation commonly adopted in comparisons with general-purpose digital approaches (*38*).

Although there is no universal algorithm for solving combinatorial optimization problems efficiently, specialized algorithms such as WalkSAT can accelerate the solution of specific problems, such as 3-SAT. We benchmark the performance of our Ising machine by comparing it with the WalkSAT algorithm because randomized algorithms such as WalkSAT with good implementations on modern computing hardware can be much faster than other heuristic methods such as simulated annealing (*35*). We implement the WalkSAT algorithm on a computer and calculate its TTS and ETS for $m/n = 3$ and plot them in the black curve in the middle and bottom panels of Fig. 4C. It shows that our Kerr-soliton Ising machine, which is designed to solve general Ising models, still takes less or the same time and consumes two orders of magnitude less optical energy than the WalkSAT algorithm.

DISCUSSION

We have demonstrated a Kerr-soliton Ising machine capable of solving combinatorial optimization problems, notably 3-SAT, with high speed and low energy consumption. Our system leverages the intrinsic bistability of Kerr microresonator solitons to encode spin states and uses a hybrid optoelectronic feedback network for fully programmable, all-to-all interactions among up to 256 spins. Each soliton bifurcates into one of two stable amplitude states under tailored feedback, providing a robust physical mechanism to emulate discrete Ising spins. By implementing gradient descent, we solve Ising-encoded SAT instances with step times as short as 3.5 μs and per-soliton power consumption of just 2.3 mW.

We benchmark the Kerr-soliton Ising machine by use of randomly generated 3-SAT problems and compare its performance against WalkSAT, a very effective heuristic solver at these problem sizes. Despite its analog nature, our system achieves comparable or better time-to-solution with two orders of magnitude lower energy use. These results underscore the potential of Kerr solitons as nonlinear, energy-efficient primitives for optical computation and position our architecture as a promising candidate for solving large-scale NP-complete problems.

Looking forward, the Kerr-soliton platform offers opportunities for photonic integration and scaling. Emerging foundry-compatible microresonator designs and monolithic integration of pulse generators and modulators on lithium niobate could markedly reduce system overhead. With electronic feedback circuits operating at 20 gigabits per second and longer resonators or faster modulation, soliton ensembles could scale to thousands of interacting spins. These advances would unlock ultrafast, analog optical coprocessors capable of accelerating optimization and inference tasks in machine learning, cryptography, and scientific computing.

MATERIALS AND METHODS

Lugiato-Lefever equation

Here we introduce the LLE with the feedback. For an ensemble of N solitons, the LLE has the form of

$$\frac{da(\theta_i)}{d\tau} = -(1+i\alpha)a(\theta_i) + i\frac{d_2}{2}\frac{\partial^2}{\partial\theta^2}a(\theta_i) + i\,|a(\theta_i)|^2\,a(\theta_i) + f(\theta_i) \tag{3}$$

where $\theta_i \in [2\pi i/N, 2\pi(i+1)/N]$, $a(\theta_i)$ is the ith soliton, α is the detuning, d_2 is the normalized second-order dispersion coefficient, and $|f(\theta_i)|^2 = |f_0(\theta_i)|^2\,(1+\xi_i)$ is the pump pulse, where ξ_i is the feedback and $f_0(\theta_i)$ is the preset pump waveform. To prevent ξ_i from exceeding the limits of the arbitrary waveform generator (AWG) input range, we truncate ξ_i to the range $[-1, 1]$ via computer control. The waveform $f_0(\theta_i)$ is chosen, such that when $\xi_i = 0, |a_i| \simeq |a_0|$.

Driving force of the Kerr soliton Ising machine

In this section, we show how the feedback loop drives the Ising machine system to the ground state.

The stable state of the Ising machine without the feedback can be written as

$$\frac{da_0(\theta_i)}{d\tau} = -(1+i\alpha)a_0(\theta_i) + i\frac{d_2}{2}\frac{\partial^2}{\partial\theta^2}a_0(\theta_i) + i\,|\,a_0(\theta_i)\,|^2\,a_0(\theta_i) + f_0(\theta_i) \tag{4}$$

The solutions to Eq. 3 indicate two states of the solitons: either excited or empty. We show the results in the "LLE simulation" in Supplementary Text. Subtracting Eq. 4 and considering $f(\theta_i) - f_0(\theta_i) \simeq \xi_i f_0^2(\theta_i)/[f(\theta_i) + f_0(\theta_i)] \simeq \xi_i f_0(\theta_i)/2$, we have

$$\frac{d\delta a(\theta_i)}{d\tau} \simeq -(1+i\alpha)\delta a(\theta_i) + i\frac{d_2}{2}\frac{\partial^2}{\partial\theta^2}\delta a(\theta_i) + i\left[\,|\,a(\theta_i)\,|^2\,a(\theta_i) - |\,a_0(\theta_i)\,|^2\,a_0(\theta_i)\right] + \frac{f_0(\theta_i)}{2}\xi_i \tag{5}$$

where $\delta a(\theta_i) = a(\theta_i) - a_0(\theta_i)$ and $\xi_i = -\eta\nabla_i H = \eta\left(-2\sum_j J_{ij}\sigma'_j - h_i\right)$. We operate the Kerr solitons with fixed detuning ($\alpha > 1$) in the anomalous regime ($d_2 > 0$) and increase η stepwise. Changing J_{ii} does not affect the spin configuration of the global minimum of H as it only adds a constant term $\sum_i J_{ii}\sigma_i^2 = \sum_i J_{ii}$ to H, and we set $J_{ii} = -0.375$ for evolution of our system through Eq. 6 in both simulation and experiments.

From Eq. 5, it is shown that when $\xi_i > 0$, the site i is driven to the soliton state and empty state otherwise. The dispersion term $i\frac{d_2}{2}\frac{\partial^2}{\partial\theta^2}\delta a(\theta_i)$ and the Kerr shift term $i\left[\,|\,a(\theta_i)|^2\,a(\theta_i) - |\,a_0(\theta_i)|^2\,a_0(\theta_i)\right]$ provide the nonlinearity needed for the system to bifurcate the states. Both the feedback ξ_i and the nonlinearity terms drive the system to the minimal energy of the Hamiltonian H.

A simplified version of update can thus be written as

$$\begin{aligned}\sigma'_{i,t+1} &= 2\mathrm{Sigmoid}_k(\xi_{i,t}) - 1\\ &= 2\mathrm{Sigmoid}_k\left[\eta_t\left(-2\sum_j J_{ij}\sigma'_{j,t} - h_i\right)\right] - 1\end{aligned} \tag{6}$$

where t is the step number and $\mathrm{Sigmoid}_k(x) = 1/(1+e^{-kx})$. We set k so the function approximates the experimental nonlinear soliton response data.

The external force term h_i is required in the Ising model form of many NP-hard problems, e.g., SAT problems, maximum independent set problems, set cover problems, and knapsack problems, etc. (*39*). This is because the QUBO form for these problems has linear term or quadratic constraints. Most constrained NP-hard problems require external field. While the way to apply the J_{ij} interactions in the feedback system is similar in this work and the coherent Ising machines (CIMs) based on optical oscillators, however, in CIMs, additional spin sources or computational costs are required to apply the external force. In (*3*), auxiliary spins are used to apply nonzero h_i, and the success probability of solving a problem is related to the number of auxiliary spins, which consumes more optical sources and increases the complexity of the system. In (*31*), although no auxiliary spins are used, the feedback term takes the form of $-2\sum_j J_{ij}\sigma'_j - h_i\,|\sigma'_j|$, which means computation of $|\sigma'_j|$ requires judgment of the sign of the spin σ'_j, adding to the computational cost. This can also add burden to the future on-chip design of the feedback loop. For the Kerr soliton Ising machine, however, it is natural to add the bias term h_i in the feedback ξ_i, since the driving force $f(\theta)$ is separate from the intracavity field $a(\theta)$ [i.e., in Eq. 3, $f(\theta_i)$ is an independent term, rather than a term multiplied with $a(\theta_i)$ for optical oscillators]. Thus, the number of solitons is just the number of spins in an Ising problem, eliminating the necessity to add auxiliary spins (or solitons) and computational costs, which keeps the optical sources constant and improves the robustness of our system.

Solutions to the 3-SAT problem from an Ising problem

We apply the method in (*32*) to translate the 3-SAT problem with n variables ($V_1 \ldots V_n$) and m clauses ($C_1 \ldots C_m$) to a QUBO problem and then convert the QUBO problem to an Ising problem with $N = m + n$ spins. After the Ising machine evolves to the final state, we obtain a spin array with N spins, and the first n spins are the solutions to the 3-SAT problem, i.e., $\sigma_i = 1 \leftrightarrow V_i = \mathrm{True}$ and $\sigma_i = -1 \leftrightarrow V_i = \mathrm{False}$.

We apply the code for the WalkSAT algorithm introduced in (*40*) on the Intel Core i7-1355U processor. We solve each SAT problem 100 times to calculate the corresponding TTS.

Variation of pump power

The variation in pump power observed in Fig. 3D can be attributed to the EDFA's automatic gain control. When the pulses first enter the EDFA, they are amplified maximally due to the absence of preceding pulses, resulting in a higher peak power. As more pulses arrive, the EDFA adjusts its gain to maintain a constant average power, leading to a gradual decrease in the peak power of the pump pulses. This, in turn, affects the soliton pulses, which initially build up and reach a maximum power before slightly decreasing with the pump pulses.

After the pump pulses stop at the 41st round trip, the soliton peaks briefly increase due to the absence of interference from incoming pump pulses but soon decay exponentially due to the lack of pump power. We note that this effect does not affect the Ising machine's ability to solve combinatorial optimization problems.

Experimental operation of the Ising machine

We operate the Ising machine with an external computer that controls the AWG and reads data from an oscilloscope. We form and send a pulse train to the AWG which repeatedly modulates the intensity modulator (IM2) at ~60 gigasamples per second and read the soliton state from the oscilloscope. Each pulse in the pulse train has a width of 135 ps. To calibrate the Ising machine, we first send a train of pulses with increasing intensity and measure the corresponding soliton intensity. By fitting the soliton intensity to the pump intensity, as shown in Fig. 2B, we determine the pulse height $|f_0(\theta_i)|^2$ that corresponds to zero feedback ($\xi = 0$). On the basis of the height, we initiate the Ising machine with pump pulses of uniform height, update the pulse height with the feedback ξ, and record the resulting soliton states. Each step takes around 0.1 s and most of the time is taken to send the pulse to the AWG and read the soliton trace from the oscilloscope. See Supplementary Text for more details on the benchmark problems we have solved and the feedback network.

When the Ising machine is running, the detuning and EDFA gain are stable. Although the room temperature is constant, the change in pump intensities can slightly drift the resonances of the fiber resonator, so the PDH locking gets unlocked around 30 min.

Number of steps for different N and m/n

For problems of different size and different clause-to-variable ratio, we apply different numbers of steps to reach a reliable success probability in a reasonable time. For the problems in Fig. 4C, we apply $N_s = 100, 100, 100, 50, 50$ for $N = 256, 192, 128, 64, 32$ and $m/n = 3$ and $N_s = 100, 100, 75, 50, 50$ for $N = 256, 192, 128, 64, 32$ and $m/n = 2$, respectively.

Numbers of variables and clauses for different spin numbers

For the spin number N, which is a power of 2, m/n cannot exactly equal to 2. For a given N, we choose the m and n, such that m/n is the closest to 2, while $m/n \geq 2$. With $m/n = 2$, $m = 22$ and $n = 10$ for $N = 32$, $m = 43$ and $n = 21$ for $N = 64$, $m = 86$ and $n = 42$ for $N = 128$, $m = 128$ and $n = 64$ for $N = 192$, and $m = 171$ and $n = 85$ for $N = 256$.

Threshold of the solitons

For continuous-wave pumping, the expression for the threshold of the solitons in a Kerr resonator is

$$P_{\mathrm{th}} = \frac{\pi n_g^2 L A_{\mathrm{eff}}}{4 n_2 \lambda Q_i^2} \frac{(1+K)^3}{K} \tag{7}$$

where Q_i is the intrinsic quality factor, Q_e is the external quality factor, $K = Q_i/Q_e$ is the coupling coefficient, n_g is the group index, n_2 is the nonlinear index, L is the circumference of the resonator, A_{eff} is the fiber effective area, and λ is the wavelength. In our experiment, $Q_i = 1.34 \times 10^9$, $Q_e = 4.61 \times 10^8$, $n_g = 1.44$, $A_{\mathrm{eff}} = 8.5 \times 10^{-11}$ m^2, $L = 29$ m, $n_2 = 3.11 \times 10^{-20}$ m^2/W, and $\lambda = 1556$ nm. The circumference L of the resonator includes the length of the SMF (25 m) and the couplers (around 2 m each). For the fiber resonator that we use, the predicted threshold is $P_{\mathrm{th}} = 0.9$ W for continuous wave pumping. Because we use a pulse pump and the width of a single pulse is around 1/2048 of a round trip, the threshold to generate a single soliton is around 0.45 mW, which is comparable to 2.3 mW measured in the experiment considering the loss after the EDFA. The use of a microcomb to generate the pulse pump would be ideal, enabling $P_{\mathrm{th}} \sim 0.05$ mW. As we increase the number of pump pulses to activate a larger soliton ensemble, P_{th} is constant.

TTS and ETS with respect to K

Here, we explore the relation of TTS and ETS with the coupling coefficient K. Since the normalized LLE (Eq. 3) does not directly include K, TTS is fundamentally determined by the time unit $2/\kappa$. Thus, we have

$$\mathrm{TTS} \propto \frac{2}{\kappa} \propto \frac{\lambda Q_i}{1+K} \tag{8}$$

Since the ETS is the energy consumed during TTS, we have

$$\mathrm{ETS} \propto \mathrm{TTS} \times P_{\mathrm{th}} \propto \frac{1}{Q_i} \frac{(1+K)^2}{K} \tag{9}$$

In our system, Q_i comes from the loss of splicing between fibers and the excess loss of the couplers, while K can be tuned by changing the coupling ratio of the couplers. From Eq. 9, the ETS reaches the minimum with $K = 1$.

Supplementary Materials

This PDF file includes:
Supplementary Text
Figs. S1 to S4

REFERENCES

1. N. Mohseni, P. L. McMahon, T. Byrnes, Ising machines as hardware solvers of combinatorial optimization problems. *Nat. Rev. Phys.* **4**, 363–379 (2022).
2. K. Tatsumura, M. Yamasaki, H. Goto, Scaling out Ising machines using a multi-chip architecture for simulated bifurcation. *Nat. Electron.* **4**, 208–217 (2021).
3. H. Takesue, K. Inaba, T. Honjo, Y. Yamada, T. Ikuta, Y. Yonezu, T. Inagaki, T. Umeki, R. Kasahara, Finding independent sets in large-scale graphs with a coherent Ising machine. *Sci. Adv.* **11**, eads7223 (2025).
4. Y. Mizuno, T. Komatsuzaki, Finding optimal pathways in chemical reaction networks using Ising machines. *Phys. Rev. Res.* **6**, 013115 (2024).
5. J. Laydevant, D. Marković, J. Grollier, Training an ising machine with equilibrium propagation. *Nat. Commun.* **15**, 3671 (2024).
6. A. Sharma, M. Burns, A. Hahn, M. Huang, Augmenting an electronic Ising machine to effectively solve boolean satisfiability. *Sci. Rep.* **13**, 22858 (2023).
7. P. L. McMahon, The physics of optical computing. *Nat. Rev. Phys.* **5**, 717–734 (2023).
8. T. Inagaki, Y. Haribara, K. Igarashi, T. Sonobe, S. Tamate, T. Honjo, A. Marandi, P. L. Mc Mahon, T. Umeki, K. Enbutsu, O. Tadanaga, H. Takenouchi, K. Aihara, K.-I. Kawarabayashi, K. Inoue, S. Utsunomiya, H. Takesue, A coherent Ising machine for 2000-node optimization problems. *Science* **354**, 603–606 (2016).
9. T. Honjo, T. Sonobe, K. Inaba, T. Inagaki, T. Ikuta, Y. Yamada, T. Kazama, K. Enbutsu, T. Umeki, R. Kasahara, K.-I. Kawarabayashi, H. Takesue, 100,000-spin coherent Ising machine. *Sci. Adv.* **7**, eabh0952 (2021).
10. Y. Yamamoto, K. Aihara, T. Leleu, K.-i. Kawarabayashi, S. Kako, M. Fejer, K. Inoue, H. Takesue, Coherent Ising machines—optical neural networks operating at the quantum limit. *npj Quantum Inf.* **3**, 49 (2017).
11. M. Babaeian, D. T. Nguyen, V. Demir, M. Akbulut, P.-A. Blanche, Y. Kaneda, S. Guha, M. A. Neifeld, N. Peyghambarian, A single shot coherent Ising machine based on a network of injection-locked multicore fiber lasers. *Nat. Commun.* **10**, 3516 (2019).
12. D. Pierangeli, G. Marcucci, C. Conti, Large-scale photonic Ising machine by spatial light modulation. *Phys. Rev. Lett.* **122**, 213902 (2019).
13. M. Prabhu, C. Roques-Carmes, Y. Shen, N. Harris, L. Jing, J. Carolan, R. Hamerly, T. Baehr-Jones, M. Hochberg, V. Čeperić, J. D. Joannopoulos, D. R. Englund, M. Soljačić, Accelerating recurrent Ising machines in photonic integrated circuits. *Optica* **7**, 551–558 (2020).

14. F. Böhm, G. Verschaffelt, G. Van der Sande, A poor man's coherent Ising machine based on opto-electronic feedback systems for solving optimization problems. *Nat. Commun.* **10**, 3538 (2019).
15. F. Böhm, D. Alonso-Urquijo, G. Verschaffelt, G. Van der Sande, Noise-injected analog Ising machines enable ultrafast statistical sampling and machine learning. *Nat. Commun.* **13**, 5847 (2022).
16. Q. Cen, H. Ding, T. Hao, S. Guan, Z. Qin, J. Lyu, W. Li, N. Zhu, K. Xu, Y. Dai, M. Li, Large-scale coherent Ising machine based on optoelectronic parametric oscillator. *Light Sci. Appl.* **11**, 333 (2022).
17. L. Quinn, Y. Xu, J. Fatome, G.-L. Oppo, S. G. Murdoch, M. Erkintalo, S. Coen, Coherent Ising machine based on polarization symmetry breaking in a driven Kerr resonator. arXiv:2411.16009 [physics.optics] (2024).
18. G. Pedretti, F. Böhm, T. Bhattacharya, A. Heittmann, X. Zhang, M. Hizzani, G. Hutchinson, D. Kwon, J. Moon, E. Valiante, I. Rozada, C. E. Graves, J. Ignowski, M. Mohseni, J. P. Strachan, D. Strukov, R. Beausoleil, T. Van Vaerenbergh, Solving Boolean satisfiability problems with resistive content addressable memories. *npj Unconv. Comput.* **2**, 7 (2025).
19. S. Chiavazzo, M. C. Strinati, C. Conti, D. Pierangeli, Ising machine by dimensional collapse of nonlinear polarization oscillators. *Phys. Rev. Lett.* **135**, 063801 (2025).
20. A. M. Dee, S. A. Moazeni, 10.8mW mixed-signal simulated bifurcation ising solver using SRAM compute-in-memory with 0.6us time-to-solution. arXiv:2504.10384 [eess.SY] (2025).
21. T. Herr, V. Brasch, J. D. Jost, C. Y. Wang, N. M. Kondratiev, M. L. Gorodetsky, T. J. Kippenberg, Temporal solitons in optical microresonators. *Nat. Photonics* **8**, 145–152 (2014).
22. T. J. Kippenberg, A. L. Gaeta, M. Lipson, M. L. Gorodetsky, Dissipative Kerr solitons in optical microresonators. *Science* **361**, eaan8083 (2018).
23. F. Leo, S. Coen, P. Kockaert, S.-P. Gorza, P. Emplit, M. Haelterman, Temporal cavity solitons in one-dimensional Kerr media as bits in an all-optical buffer. *Nat. Photonics* **4**, 471–476 (2010).
24. T. E. Drake, T. C. Briles, J. R. Stone, D. T. Spencer, D. R. Carlson, D. D. Hickstein, Q. Li, D. Westly, K. Srinivasan, S. A. Diddams, S. B. Papp, Terahertz-Rate Kerr-Microresonator Optical Clockwork. *Phys. Rev. X* **9**, 031023 (2019).
25. J. Zang, T. C. Briles, J. S. Morgan, A. Beling, S. B. Papp, Universal electronic synthesis by microresonator-soliton photomixing. arXiv:2505.08707 [physics.optics] (2025).
26. D. C. Cole, E. S. Lamb, P. Del'Haye, S. A. Diddams, S. B. Papp, Soliton crystals in Kerr resonators. *Nat. Photonics* **11**, 671–676 (2017).
27. A. Spott, E. J. Stanton, N. Volet, J. D. Peters, J. R. Meyer, J. E. Bowers, Heterogeneous integration for mid-infrared silicon photonics. *IEEE J. Sel. Top. Quantum Electron.* **23**, 8200810 (2017).
28. H. Liu, I. Dickson, A. Antohe, L. G. Carpenter, J. Zang, A. R. Carollo, A. Dan, J. A. Black, S. B. Papp, Implementing photonic-crystal resonator frequency combs in a photonic foundry. *Opt. Lett.* **50**, 2570–2573 (2025).
29. Y. K. Chembo, Quantumdynamics of Kerr optical frequency combs below and above thresh old: Spontaneous four-wave mixing, entanglement, and squeezed states of light. *Phys. Rev. A* **93**, 033820 (2016).
30. C. Godey, I. V. Balakireva, A. Coillet, Y. K. Chembo, Stability analysis of the spatiotemporal Lugiato-Lefever model for Kerr optical frequency combs in the anomalous and normal dispersion regimes. *Phys. Rev. A* **89**, 063814 (2014).
31. H. Takesue, K. Inaba, T. Inagaki, T. Ikuta, Y. Yamada, T. Honjo, T. Kazama, K. Enbutsu, T. Umeki, R. Kasahara, Simulating Ising Spins in External Magnetic Fields with a Network of Degenerate Optical Parametric Oscillators. *Phys. Rev. Appl.* **13**, 054059 (2020).
32. J. Nüßlein, T. Gabor, C. Linnhoff-Popien, S. Feld, Algorithmic, QUBO formulations for k-SAT and hamiltonian cycles, in *Proceedings of the Genetic and Evolutionary Computa tion Conference Companion* (Association for Computing Machinery, 2022), pp. 2240–2246 (2022); https://doi.org/10.1145/3520304.3533952.
33. J. Zang, J. S. Morgan, A. Beling, S. B. Papp, Broadband optoelectronic mixer for terahertz frequency-comb measurements. *Opt. Lett.* **50**, 3173–3176 (2025).
34. B. Selman, H. Kautz, Domain-independent extensions to GSAT: Solving large structured satisfiability problems, in *Proceedings of the 13th International Joint Conference on Artifical Intelligence* (Morgan Kaufmann Publishers Inc., 1993), vol. 1, pp. 290–295.
35. B. Selman, H. A. Kautz, B. Cohen, Noise strategies for improving local search, in *Proceedings of the Twelfth National Conference on Artificial Intelligence* (American Association for Artificial Intelligence, 1994), vol. 1, pp. 337–343.
36. J. M. Crawford, L. D. Auton, Experimental results on the crossover point in random 3-SAT. *Artif. Intell.* **81**, 31–57 (1996).
37. T. Bhattacharya, G. H. Hutchinson, G. Pedretti, X. Sheng, J. Ignowski, T. Van Vaerenbergh, R. Beausoleil, J. P. Strachan, D. B. Strukov, Computing high-degree polynomial gradients in memory. *Nat. Commun.* **15**, 8211 (2024).
38. T. Leleu, F. Khoyratee, T. Levi, R. Hamerly, T. Kohno, K. Aihara, Scaling advantage of chaotic amplitude control for high-performance combinatorial optimization. *Commun. Phys.* **4**, 266 (2021).
39. A. Lucas, Ising formulations of many NP problems. *Front. Phys.* **2**, 5 (2014).
40. S. Russell, P. Norvig, AIMA Python: Python implementation for artificial intelligence: A modern approach—WalkSAT (Github); https://github.com/aimacode/aima-python. Accessed 29 October 2025. n.d.

Acknowledgments: We thank L. Williams and S. Yeola for the technical review of the paper and the DARPA QuICC program management team for helpful comments throughout the experiments. **Funding:** This research has been funded by the DARPA QuICC program, AFOSR FA9550-20-1-0004 project number 19RT1019, and NIST. This work is a contribution of the US government and is not subject to copyright. Mention of commercial products used in the research is for informational purposes only and does not represent an endorsement. **Author contributions:** Y.J. and S.B.P. conceived the project and wrote the paper. Y.J. and N.C. designed the experiment setup. Y.J., N.C. and J.Z. performed the experiment and collected the data. P.C. provided the benchmark SAT problems and the benchmark code for WalkSAT. Y.J. and B.E. conceived the feedback network of the Ising machine and the algorithm for the feedback update. F.A. provided the insight for the design of the digital feedback. F.A. and S.B.P. supervised the project. **Competing interests:** There are no competing interests to declare. **Data, code, and materials availability:** All data and code needed to evaluate and reproduce the results in the paper are present in the paper and/or the Supplementary Materials. No new materials were generated in this study.

Submitted 26 August 2025
Accepted 16 April 2026
Published 22 May 2026
10.1126/sciadv.aeb7930

Science Advances

Combinatorial optimization with Kerr solitons

Yan Jin, Nitesh Chauhan, Jizhao Zang, Brian Edwards, Pratik Chaudhari, Firooz Aflatouni, and Scott B. Papp

Sci. Adv. **12** (21), eaeb7930. DOI: 10.1126/sciadv.aeb7930

View the article online
https://www.science.org/doi/10.1126/sciadv.aeb7930
Permissions
https://www.science.org/help/reprints-and-permissions

Science Advances (ISSN 2375-2548) is published by the American Association for the Advancement of Science. 1200 New York Avenue NW, Washington, DC 20005. The title *Science Advances* is a registered trademark of AAAS.